Root Cause Analysis of Solar Cell Cracks at Shingle Joints

[1,2,]*Nils Klasen, [1,3]Friedemann Heinz, [1]Angela De Rose, [1]Torsten Roessler, [1]Achim Kraft, [1,2]Marc Kamlah

[1]Fraunhofer Institute for Solar Energy Systems ISE, Heidenhofstr. 2, 79110 Freiburg, Germany

[2]Karlsruhe Institute of Technology KIT, Institute for Applied Materials – Materials and Biomechanics, Hermann-von-Helmholtz 1, 76344 Eggenstein-Leopoldshafen, Germany

[3]University of Freiburg, Institute for Sustainable Systems Engineering (INATECH), Emmy-Noether-Str. 2, 79110 Freiburg, Germany

*corresponding author: Nils Klasen, nils.klasen@ise.fraunhofer.de

Keywords: Shingle Solar Cell Interconnection, Fracture Analysis, Finite Element Method

Abbreviations[1]

1 Abstract

Photovoltaic modules with shingle solar cell interconnection experience increasing market shares in the recent years. Despite additional effort in manufacturing for separation and handling a larger number of smaller solar cells, they offer major advantages like high power densities, reduced optical and electrical losses and a highly aesthetic appearance. However, the direct cell to cell interconnection formed by electrically conductive adhesives (ECAs) still holds some challenges regarding a deeper understanding of long-term stability effects.

[1]
CTE: Coefficient of Thermal Expansion
DMA: Dynamic Mechanical Analysis
ECA: Electrically Conductive Adhesive
EL: Electroluminescence
EVA: Ethylene-Vinyl Acetate
FEM: Finite Element Method
FS: Front Side
PL: Photoluminescence
pSPEER: p-type Shingled Passivated Edge Emitter and Rear (Solar Cell)
RS: Rear Side
SEM: Scanning Electron Microscopy
TC: Thermal Cycling
TTS: Time Temperature Superposition
WLF: Williams-Landel-Ferry

In this work, we report the root cause of cracks occurring on shingle solar cells in PV modules subjected to thermal cycling. Experimental investigations of six different ECAs show that the positions of cracks are precisely limited to the applied ECA in the joint and the occurrence confined to the rear side of the solar cells. Structural mechanic simulations based on the Finite Element Method (FEM) obtain maximum stresses of up to $400\ \mathrm{MPa}$ on the rear surface of the solar cell orientated towards the back sheet. On the opposing surface, orientated towards the glass, the stresses are on a far lower level at around $230\ \mathrm{MPa}$. We measured the characteristic fracture stresses and found values of $96\ \mathrm{MPa}$ on the rear and $265\ \mathrm{MPa}$ on the front side of the separated shingle solar cells. The lower values on the rear originate from microfractures at the solar cell edges caused by the laser scribe and mechanical cleave process.

We discuss two mechanisms taking place at the shingle joint during cooling from lamination temperature at $160\ ^{\circ}\mathrm{C}$ to $-40\ ^{\circ}\mathrm{C}$. First a relative shift of the solar cells caused by a mismatch in the thermal expansion in y-direction. Second a mismatch in thermal expansion in z-direction. We apply an anisotropic thermal expansion behavior in our simulations to separate both mechanisms and reveal the driving mechanism behind crack formation. We find that the cracks are caused by thermal contraction of the encapsulant in z-direction. Transversal contraction of the encapsulant causes additional strain in z-direction.

2 Introduction

Over the last five years the diversity in solar module technologies increased significantly. Besides new solar cell architectures we also see major changes in the field of interconnection. One innovative approach is the shingle interconnection, where solar cells are bonded directly front to rear by slightly overlapping them at the edges. This not only increases the active module area, but also minimizes ribbon shading losses. Since the solar cells are cut into fifth or sixth parts, the current per string and with it the power loss due to ohmic heating is reduced. In summary, the shingle technology promises high power density solar modules while at the same time offering a valuable aesthetic look by avoiding the visible metal ribbons and solar cell gaps.

This makes shingle solar modules well suited for integrated applications e.g. in buildings and vehicles where both, power density and appearance, are of great importance. For these specific applications, there is a huge potential of around 1400 GW only in Germany [1]. However, along with the promising properties also new technological challenges arise. Due to the huge variety of environmental impacts and climatic conditions the long-term stability in general is a challenging aspect of photovoltaic devices.

Alternating temperatures cause thermomechanical stresses inside the laminate and relative movements of the solar cells [2]. For the latter, ribbon interconnection compensates within the gap between adjacent solar cells. In shingle solar modules the ECAs, applied for joint formation, as well as the solar cells themselves undergo deformations. In experiments we observed crack patterns with a strong correlation to the pattern of applied ECA.

In this work, we present detailed investigations, to clarify the origin of the observed cracks. We first discuss the crack occurrence in thermal cycling experiments of solar module samples built with six different ECAs. Structural mechanic simulations based on the Finite Element Method (FEM) complement the experimental work and are used to identify the root cause of crack formation. The characteristic fracture stress of the solar cells used is determined according to DIN SPEC 91351 [3] and used to asses both experimental and numerical results.

3 Experimental Investigations of Solar Cell Cracks in shingle modules

Sample preparation and experimental setting

The six different ECAs used in this screening are based on different polymer chemistries and contain varying filler particles (element and shape). *refers to defect counts on the front side † Measured by EDX on cross sections

Table 1 summarizes the experimental groups and their respective ECA properties. For each group we built four modules subjected to thermal cycling and one non aged reference. Each module contains seven bifacial pSPEER shingle solar cells [4] (edge length $148\ \mathrm{mm}\ x\ 23\ \mathrm{mm}$). We applied ECA via stencil printing with a $100\ \mu\mathrm{m}$ thick stainless steel stencil and the printing pattern shown in Figure 1a. The eight printed ECA pads per joint are $16\ \mathrm{mm}$ wide and separated by a $2\ \mathrm{mm}$ gap. Hence in total, there are 48 ECA pads per module. For overlap control we use a stainless steel positioning device [5]. After assembly, the samples are cured at $150\ °\mathrm{C}$ with curing times specified in the data sheets. We used optimized string interconnectors to reduce mechanical stress and connected them with eutectic Sn63Pb37 solder. For module integration we used an ethylene-vinyl acetate (EVA) encapsulant, a transparent PPE back sheet and $3.2\ \mathrm{mm}$ float glass. Lamination takes place in a plate-membrane laminator at $160\ °\mathrm{C}$ and $9\ \mathrm{min}$ compression with ambient pressure.

Group	Polymer	Filler material	Particle shape	# cracks TC100	# cracks TC1000
A	Acrylate	Ag	Spheres	4	4
B	Acrylate	Ag	Flakes	0	0
C	Epoxy Carboxylate	Cu/Ag	Flakes/Flakes	59	59
D	Epoxy Carboxylate	Cu (Ag-coated)	Flakes	12	13
E	Cycloaliphatic Epoxy	Cu (Ag-coated)	Flakes	75+1*	97+2*
F	$< 5\ \%_{wt}$†	Ag	Flakes/Spheres	4	6

*refers to defect counts on the front side † Measured by EDX on cross sections

Table 1: Summary of adhesives used in the screening study and defect counts after TC100 and TC1000

After initial characterization with electroluminescence (EL) and IV power rating, the samples were aged in an accelerated thermal cycle test with $4\ \mathrm{K\,min^{-1}}$ temperature change. At the extremal values ($-40\ °\mathrm{C}$ and $+85\ °C$), the temperature was kept constant for $20\ \mathrm{min}$, which was monitored *in-situ* by solar modules with integrated thermocouples placed between the samples. Previous work by Schiller

et al shows, that there are no detectable differences in the results of this procedure compared to the rate of $1.6\ \mathrm{K\ min^{-1}}$ defined in IEC 61215 [6].

The modules where exposed to 1000 TC cycles with intermediate characterization steps at 100, 200, 400, 600, 800, 1000 cycles by EL-imaging and IV power rating. After the final characterizations 85 metallographic specimens were prepared from selected samples and positions for investigation with light microscopy and Scanning Electron Microscopy (SEM). We took samples from the non-aged reference and from the aged modules out of each group. Cross section specimens were embedded in an epoxy resin with conductive carbon filler particles to enhance charge carrier drain in SEM investigations.

Defect Characterization

Figure 1a shows a photoluminescence image (PL) of a shingle module after TC1000 featuring a distinct pattern of areas with low PL intensity and a clear local correlation to the applied ECA. Figure 1b shows a microscopic image of the solar cell surface at an exemplary position. A crack in the solar cells is responsible for the areas of low PL intensity. We did not find such cracks before ageing in any of the modules. Thus, an origin from manufacturing can be excluded. Since distinct gaps between single cracks allow a precise assignment to the subjacent ECA pads, we count the number of cracks per module and group respectively. Besides the experimental set-up, Table 1 shows the number of cracks in EL after TC100 and TC1000 for all experimental groups. The values refer to the total count over the aged modules of one group. In total we found 182 defects from which 180 were located on the rear side of the solar cells. Only one module in group E showed two cracks on the front side of the cells. Since there are no significant differences in the appearance of the cracks, we conclude, that it is linked to the shingle joint in general. However, we see significant differences in the crack counts between the groups, which also indicates, that ECA properties influence the occurrence. We found one group (ECA B) to not feature this specific cracking behavior at all.

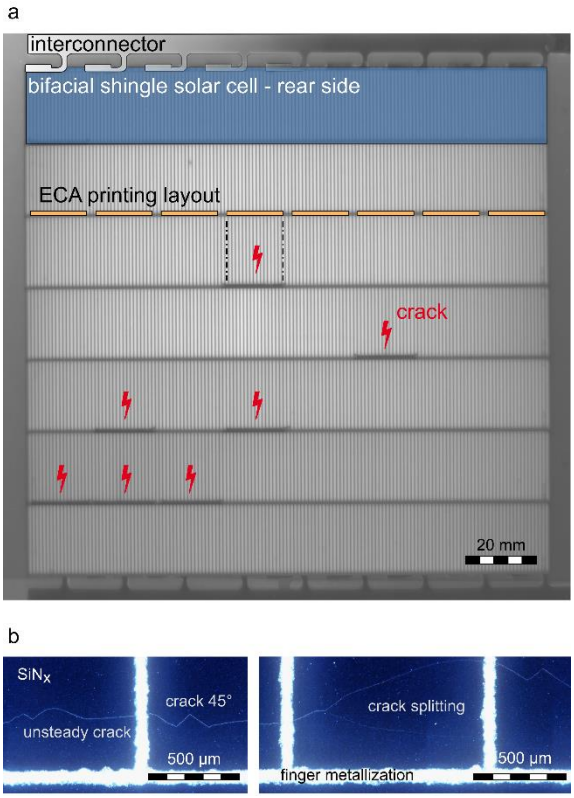

Figure 1: **a** Rear side photoluminescence image of a shingle module consisting of seven bifacial solar cells after 1000 thermal cycles. The yellow overlay sketches the ECA present in the overlap. **b** Top view darkfield microscopy images show the crack propagation close and in parallel to the edge on the solar cell surface.

In our experiments the cracks formed prior to completing 100 thermal cycles. The number of cracks was stable from then on and only in single cases we observe additional cracks to appear between TC100 and TC1000. So far, the occurrence was mostly limited to the rear side of the solar cells and thus is detectable only on bifacial solar cells in combination with a transparent back sheet. The EL analysis showed that the cracks propagate in parallel to the solar cell edges, which is atypical for monocrystalline silicon solar cells. The anisotropy of silicon leads to preferred failure directions linked to the crystal planes found in its diamond lattice. Fractures preferably occur along the <111> plane, closely followed by the <110> plane [7]. Solar cell wafers are commonly oriented in <100> respectively <010> orientation along their edges with a <001> surface normal. Hence fractures preferably are found under $45°$ angles towards the wafer edges.

Microscopy examinations in darkfield mode (Figure 1b) resolve a mixed fracture progression. In parts the cracks feature the expected $45°$ orientation. However, there are also wide sections where there is no distinct direction detectable. Splitting and merging of the cracks is observed as well as the before mentioned distinct gaps between two cracks where no ECA is printed in the cell overlap. At these gaps, also visible in both EL and PL the crack tips expand towards the wafer edges and center under the characteristic $45°$ angle. The combination of all findings indicates high tensile stresses and sudden failure rather than a steady growth along the <111> planes.

Defect stability and link to losses in power

Figure 2 shows two exemplary series of EL images for two modules of group D and F before thermal cycling, after TC 100 and after TC 1000. Additional occurred cracks are marked with an "x" in the images. As pointed out above, the cracks mostly appear between initial state and TC100. We only find exceptions from this in group D, where additional cracks appear between TC100 and TC1000. Regions of cracking are distinguishable from each other by a distinct gap in between, where there is no ECA present in the joint. Also, the characteristic tips towards the cell center and edges are visible.

Figure 2: Exemplary electroluminescence images from the rear side of two bifacial shingle modules of group D and F at TC0, TC100 and TC1000. In each image additional occurred cracks are marked by an "x". The overlay boxes contain the STC power rating P, fill factor FF and the crack count n.

We observe up to 29 cracks per module in group D. The exemplary series of EL images in Figure 2 shows the evolution of number of cracks, STC power rating and fill factor. For this particular module, we find losses in power of 1% despite the larger number of cracks. The fill factor is reduced by $1.2\ \%$ and shows that the losses are linked to an increased series resistance of the interconnection rather than cracks, which cause losses by isolating parts of the solar cell and hence cause a reduction of current. The average power ratings of the entire group display values of $(-1.1 \pm 0.7)\ \%$ after TC100 and $(-8.9 \pm 5.8)\ \%$ after TC1000. At the same time also the fill factor reduces by $(-1.0 \pm 0.3)\ \%$ after TC100 and $(-9.0 \pm 5.7)\ \%$ after TC1000. Although this group in total shows significant degradation after TC1000, the losses again are linked to an increase in series resistance and not to a current reduction caused from solar cell chippings ($\Delta I_{sc} = 0$).

We find similar correlations in group F. Again, a large number of cracks (26 out of 48 ECA pads) are found in the module with a power degradation of $0.6\ \%$ after TC1000. In contrast to group D, also the average power degradation is much lower: $(-1.1 \pm 0.3)\ \%$ after TC100 and $(-2.3 \pm 1.5)\ \%$ after

TC1000. Again, losses in the fill factor, (-1.1 ± 0.3) % after TC100, and (-2.6 ± 1.3) % after TC1000, are responsible for the losses in power.

Additionally, the overall low losses in power after TC100 and large number of cracks already present in both groups exclude the cracks from being responsible for significant power losses. However, already existing cracks are likely to propagate when combined with mechanical loads. Propagating cracks then could lead to electrical isolation of parts of the solar cells leading to more severe power losses.

SEM analysis

Examinations of metallographic specimens using SEM show, that the fissures start from the rear side of the lower solar cell at the shingle joint and propagate towards the ECA. Figure 3a and b show an overview and detail of an exemplary cross section. We find these cracks in samples cut from positions showing the defect in EL. At reference positions without indication in EL we do not find such cracks in cross section examinations. Hence, we can exclude any impact from sample preparation on the observed fissures. We find smaller chippings from grinding and polishing at the solar cell – encapsulant interfaces, which however do not interfere with the investigated failures.

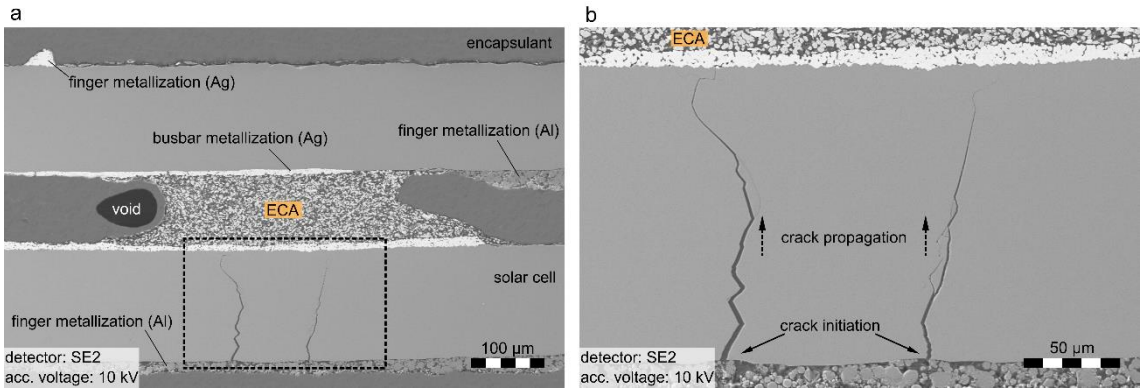

Figure 3: **a** Exemplary cross section SEM image of a metallographic specimen dissected from a sample after TC1000 showing the overlap region of two shingle interconnected solar cells. **b** The close up SEM image of the framed area in a shows the crack initiation on the rear side and propagation towards the front side. Note that the cross section by chance intersects along an Al-finger of the rear side metallization of the lower solar cell.

Conclusions from the experimental investigations

Analysis of defect occurrence in EL in combination with power ratings and investigation of metallographic specimens with SEM at shingle modules with six different ECAs lead to the following findings.

- **There are (mechanical) properties of the ECA which favor or mitigate the crack formation.** Between the investigated ECAs there are significant differences in the number of cracks observed. The mechanical stiffness and the CTE are key properties for the thermal expansion behavior and therefore likely to be relevant for the mechanism.
- **The root cause is linked to the shingle joint or the laminate in principle.** A wide range of ECAs develop cracks with an identical appearance.

- **High tensile stresses are involved.** The mixed fracture course of the cracks and the observation of cracks on the full ECA pad area indicates a sudden and complete crack formation rather than a controlled growth over many cycles.
- **The defect count is in most cases stable after first occurrence and often occurs prior to 100 thermal cycles.**
- **The defect is mostly limited to the solar cell rear side.**
- **The experiments establish no link to significant losses in power.** This might change when mechanical loads occur in the field. However, due to the size effect this cannot be investigated on laboratory scale sampled. Differences might arise for full-sized module.

4 Characteristic Fracture Stress Determination of Solar Cells

Silicon is a brittle material; hence it fails without plastic deformation when tensile stresses exceed a critical stress level. Microscopic flaws and already existing defects e.g. from manufacturing lead to a statistically distributed failure stress, best described by the Weibull distribution P_f (Eq.(1)) [8]. For silicon based devices this was shown by Hauck et al [9], Paul et al [10] and later also used on solar cells [11] and solar modules [12].

$$P_\mathrm{f} = 1 - e^{-\left(\frac{\sigma}{\sigma_\mathrm{c}}\right)^m} \tag{1}$$

P_f is a statistical quantity giving failure rates or failure propabilities e.g. in brittle materials amongst many other applications in engineering. In Eq. (1) σ_c is the characteristic fracture stress or Weibull scale parameter and m the Weibull modulus. Tensile stresses equal to σ_c result in a $63.2\ \%$ chance of failure. The shape of the distribution around σ_c as well as its width are defined by the Weibull modulus.

The experimental evaluation of the fracture behavior is done by destructive four-point bending testing according to DIN SPEC 91351 on a *Zwick Roell* zwicki Z0.5 TN. We used > 60 solar cells per group [3] and a configuration of $L_1 = 40\ \mathrm{mm}$ and $L_2 = 80\ \mathrm{mm}$ for the distances of the inner and outer bars respectively. The pre-force was set to $0.1\ \mathrm{N}$ since the given $0.5\ \mathrm{N}$ in the standard are defined for full sized wafers and we use 1/5$^{\mathrm{th}}$ shingle solar cells. From the measured data we evaluated the Weibull parameters by using the maximum likelihood method as described in DIN EN 843-5 [13].

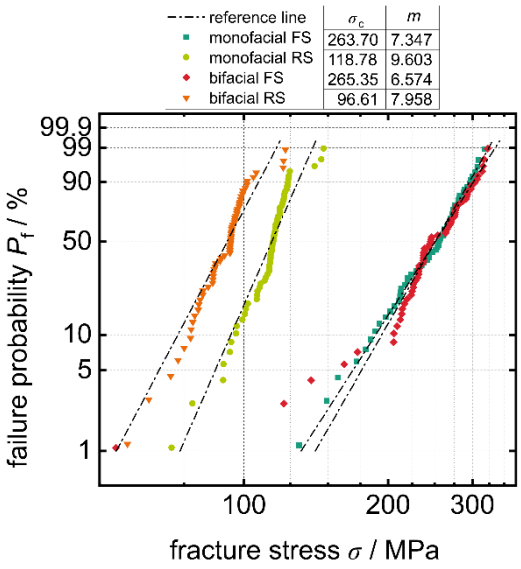

Figure 4: Measured Weibull distribution of mono- and bifacial PERC solar cells tested for tensile stresses on front (FS) and rear side (RS). The legend includes the Weibull scale factor σ_c and modulus m of each group.

Figure 4 shows the results of the fracture stress experiments with the probability of device failure P_f in dependency of the stress σ. We find no relevant differences in fracture behavior on the front side (FS) of the tested mono- and bifacial solar cells. We obtain $\sigma_{c,mono} = (263.70 \pm 4.78)$ MPa and $\sigma_{c,bifa} = (265.35 \pm 5.22)$ MPa. The rear side (RS) features significantly lower characteristic fracture stresses with $\sigma_{c,mono} = (118.78 \pm 1.62)$ MPa and $\sigma_{c,bifa} = (96.61 \pm 1.66)$ MPa. This is in agreement to work by Kaule et al. who found mechanical damages caused by the laser process to reduce the characteristic fracture stress on the rear side of the solar cells [14]. Furthermore, the absolute values for the characteristic fracture stresses are in agreement with previous work from Kaule, Eiternick et al. [15, 16].

The reduced characteristic fracture stresses found for the solar cell rear sides are a possible answer to the defect accumulation, since the fracture behavior undoubtedly is influenced by the separation process [14]. Eiternick *et al*. showed, that damage from laser ablation significantly reduces the characteristic fracture stress [16] due to microcracks at the laser groove edges. These damages however are limited to the surface of laser ablation. Accordingly, the reduced characteristic fracture stresses result from promotion of existing microcracks during testing. Thus, in real applications it requires tensile stresses close to the edges to lead to the same result. As will be shown in section 5, high tensile stresses occur very close to the wafer edges. Since we cannot specify the extent of the laser induced damages at the wafer edges, they could contribute to a crack initiation. If that were the case, a thermal laser separation process (TLS) would offer a possibility to reduce cracking.

5 Simulation studies

To further investigate the root cause of the observed cracks in shingle solar cells, we performed structural mechanical simulations based on the Finite Element Method (FEM) in the commercially available *Comsol Multiphysics* code.

In our studies, a three-dimensional model of a PV module incorporating five shingle solar cells as well as a pseudo two-dimensional cross section as shown in Figure 5 are used. The term “pseudo 2D” refers to the fact, that the model features a third dimension. However, in x-direction the geometry expands only one mesh element in depth, which allows the consideration of the anisotropy of silicon and a high-resolution mesh in the overlapping region. We simulated the cooling from the lamination temperature at $160\ °C$ to $-40\ °C$ as the extremum in accelerated ageing tests according to the IEC 61215 standard [17] for thermal cycling. Since the cooling process starts at lamination temperature, residual stresses from module manufacturing are considered in the simulations.

For discretization of the geometry, we chose hexahedral serendipity elements with a quadratic shape function. Only exclusion from this is the encapsulant domain in the 3D model, which uses a free tetrahedral mesh, again with a quadratic shape function. We used an yz-plane symmetry in the 3D geometry to reduce the computational effort. For the pseudo 2D geometry we assumed plane strain conditions in the yz-plane on both faces. Fixed and floating bearing constraints on selected points suppress rigid body motion. All constraints are sketched in red colors in Figure 5. Note, that for better visibility, both symmetry and plane strain condition are not shown on the entire surface.

We consider features of the laminate down to the busbar metallization and exclude the finger metallization which has no relevant impact on the response of a solar module to thermal loading [18]. Furthermore, we neglect the string interconnection at the module edges and focus on the periodical sequence of shingle joints. Dimensions of the material domains are given in * provided by manufacturer ** values refer to “below | above” glass transition †measured

Table 2.

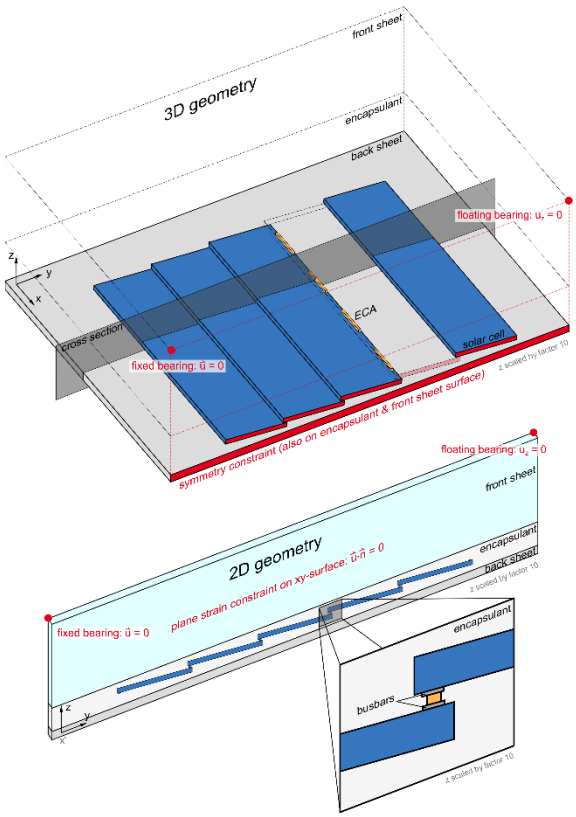

Figure 5: Three- and two-dimensional model geometries used for structural mechanics simulations based on the FEM. Highlighted in red are the boundary conditions used to constraint the model. Note, that for better visibility the z-dimension is scaled by factor 10 and one of the five solar cells is masked to show the ECA printed in the overlap.

Without discussing the constitutive equations and strategy for solving boundary value problems in detail, we introduce the displacement vector $\vec{u}$ as the solution of our FEM models, containing the displacements of each node of the mesh discretizing the model geometry. From $\vec{u}$ all other quantities are computed e.g. σ_{I}, the first principal stress, which is the maximum normal stress found in a point of the solution. $\sigma_{\mathrm{x/y/z}}$ refer to normal stresses along the axes of the cartesian coordinate system.

5.1 Material models

Float glass and monocrystalline silicon are well known materials and a variety of literature regarding their mechanical properties exists [19, 20]. Mechanical properties of silver based busbar metallization's have been studied by Wiese et al [21]. Polymeric materials on the other hand feature a great variance in their mechanical properties and are best characterized for each individual material. Eitner found that linear elastic behavior is a good approximation for *Tedlar* based multi-layer back sheets in the investigated temperature regime [2]. All material properties are included in Table 2.

Domain	Dimension	Material	Material model	Youngs modulus / GPa	Poisson's ratio / 1	CTE / 10^{-6} K^{-1}
Front sheet	z: 3.2 mm	Float glass	linear elastic	70*	0.2*	9*
Solar cells	x/y/z: 148 mm x 23 mm x 0.18 mm	Monocrystalline silicon	anisotropic linear elastic	Elasticity matrix [20, 22]		T-dep [23, 24]
Busbars	y/z: 800 µm x 20 µm	Silver (paste)	linear elastic	7.0 [21]	0.37 [25]	9.8 [21]
Electrically conductive adhesive (ECA)	x/y/z: 10 mm x 0.5 mm x 0.05 mm	Particle filled epoxy resin	linear viscoelastic	Shear relaxation spectrum † [26]		50 | 250 ** †
Encapsulant (solar cells embedded)	z: 0.9 mm	Ethylene-vinyl-acetate copolymer (EVA)	linear viscoelastic	Shear relaxation spectrum † [26]		90 | 270 [2, 27]
Back sheet	z: 0.3 mm	Tedlar-polyester-Tedlar (TPT)	linear elastic	3.5 [2]	0.29 [2]	50.4 [2]

* provided by manufacturer ** values refer to "below | above" glass transition †measured

Table 2: Reference model dimensions and material properties in FEM simulations. Note that the 2D geometry extracts a yz cross section of the 3D geometry. More details on the anisotropic and viscoelastic models can be found in the appendix.

Linear viscoelastic properties

The encapsulant ethylene-vinyl acetate copolymer (EVA) and the ECAs interconnecting the shingle solar cells show a more complex mechanical behavior. Previous work dedicated to the viscoelastic nature of both materials results in a generalized Maxwell representation (Eq. (2)) for the shear relaxation spectra $G(t)$ [26]. In Eq. (2) G_0 is the long-term elastic modulus and G_i the instantaneous modulus in the n-th Maxwell element with its characteristic relaxation time τ_i. For more detailed information on both measurement and evaluation procedure we refer to our previous contribution [26], work by Springer and Bosco [28] or literature on the fundamentals of viscoelasticity [29–32].

$$G(t) = G_0 + \sum_{i=1}^{n} G_\mathrm{i} \exp\left[-\frac{t}{\tau_\mathrm{i}}\right] \tag{2}$$

$$\log\left(a_\mathrm{T}\right) = \frac{C_1 (T - T_\mathrm{ref})}{C_2 + T - T_\mathrm{ref}} \tag{3}$$

The temperature and frequency dependent complex shear modulus of the ECA used in the FEM studies was measured at *NETZSCHs* application laboratory in Ahlden, Germany by dynamic mechanical analysis (DMA) in an *NETZSCH Gabo* Eplexor500N from $-80\ °\mathrm{C}$ to $160\ °\mathrm{C}$ in steps of $3\ \mathrm{K}$. Isothermal frequency variations from $0.5\ \mathrm{Hz}$ to $50\ \mathrm{Hz}$ in 11 logarithmic distributed steps were performed for each temperature. From the obtained data we constructed so called master curves by applying the time-temperature-superposition (TTS) principle. We used the Williams-Landel-Ferry equation (Eq. (3)) [33] to represent the shift factors $\log(a_\mathrm{T})$. We used C_1 and C_2 as fit parameters and adjusted T_ref to the glass transition temperature T_g of the polymer. This approach requires simplifying assumptions like thermorheological simplicity of the material and a homogeneous material phase. In the strict sense, this is neither the case for a particle filled polymer (ECA) nor for the semicrystalline copolymer encapsulant. However, this procedure is commonly accepted in this field and is widely used [28, 34–36].

Coefficients of thermal expansion

We measured the temperature dependent coefficient of thermal expansion α (CTE) of the ECA in a *Netzsch* TMA 402 F1/F3 Hyperion® dilatometer from $-90\ °\mathrm{C}$ to $160\ °\mathrm{C}$ with a heating rate of $2\ \mathrm{K\,min^{-1}}$ and an initial soaking time of $30\ \mathrm{min}$. From the data we calculated the differential coefficient of thermal expansion (Eq.(4)) according to ISO 11359-2 [37]. L is the specimen length at time t, T the temperature respectively and L_0 the initial sample length.

$$\alpha = \frac{dL/dt}{dT/dt} \cdot \frac{1}{L_0} \tag{4}$$

5.2 Root cause for solar cell cracking at shingle joints

Figure 6 gives an overview of the solutions of the FEM analysis at $-40\ °\mathrm{C}$. Details of both the 3D and the 2D solution plotting σ_I on the surface of the solar cells are shown in an identical color code. Note, that for better visibility in case of the 3D model the z-coordinate is scaled by factor 10, while in the 2D model the displacement vector $\vec{u}$ is scaled by factor 3. Encapsulation materials in both cases are masked or sketched.

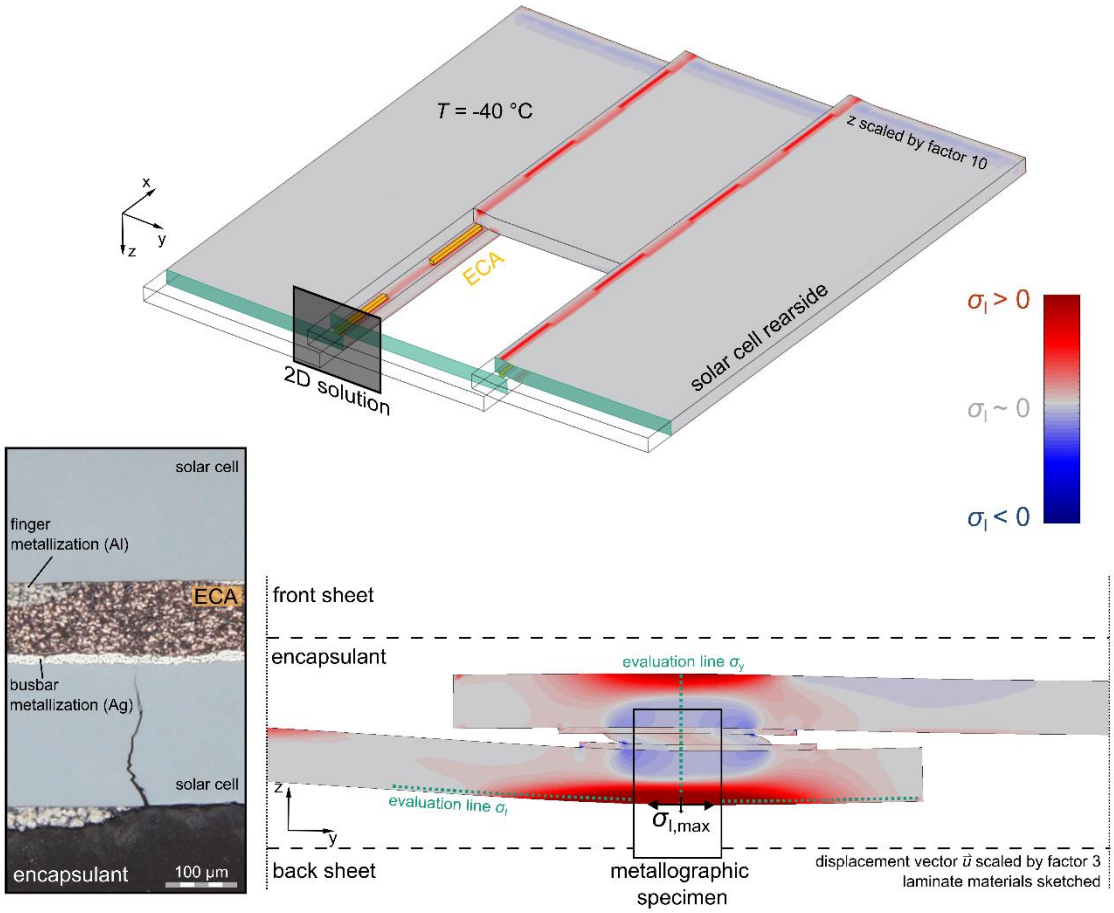

Figure 6: Solutions of the FEM models plotting the first principal stress σ_{I} at $-40\ °C$. The color code is valid for both solutions. The 3D solution shows three out of five solar cells and the ECA printed in the joint. Note that the z coordinate is scaled by factor 10 and mind the symmetry condition, highlighted in green. The 2D solution depicts a detail of one joint including the solar cells, busbar metallization and ECA. Note that its displacement vector $\vec{u}$ is scaled by factor 3 and the remaining materials of the laminate are sketched. Evaluation paths for σ_{I} along the rear side of the lower solar cell and σ_{y} intersecting the joint in vertical direction are sketched (green dotted lines). An exemplary microscope image of a metallographic specimen after TC1000 resolves the region around the joint with focus on the lower solar cell.

In the 3D solution we find regions of high tensile stresses restricted tightly to the area filled with ECA in the underlying joint. This locally constrained stress distribution explains the distinguishable gaps between the cracks found in luminescence imaging even when the gaps are only $2\ \mathrm{mm}$ wide. Nevertheless, we also find tensile stresses in the FEM model bridging the gaps, although they are significantly lower. Still in some cases they lead adjacent cracks merging (Figure 2).

Asymmetric stress distributions

A distinct asymmetry in the stress distribution with tensile stresses accumulating on the rear surface of the joint is visible in the 2D solution (Figure 6). The orientation of tensile stress around its peak value follows the solar cell surface and thus establishes an ideal baseline for crack initiation just below the ECA. The metallographic specimen shows the characteristic crack course starting from the rear side and heading towards the joint center.

Evaluations of σ_{I} along the rear side of the solar cell show the buildup of the stress during cooldown in Figure 7a. We highlight relevant temperatures, such as glass transisition temperature for both encapsulant ($T_{\mathrm{g,EVA}} = -20\ °\mathrm{C}$) and ECA ($T_{\mathrm{g,ECA}} = 60\ °\mathrm{C}$) as well as room temperature by black, differently intermitted lines. At $-40\ °\mathrm{C}$ $\sigma_{\mathrm{I,max}}$ reaches a maximum value of $390\ \mathrm{MPa}$ in the center of the joint. On the front side (Figure 7b), we find a maximum value of $232\ \mathrm{MPa}$. On the frontside the stress accumulation peak expands over roughly $1\ \mathrm{mm}$ in y-direction, while it spreads over nearly $2\ \mathrm{mm}$ on the rear side. Since both σ_{max} and the affected area are larger on the rear side compared to the front side, we find this to be the reason for crack accumulation on the solar cell rear side.

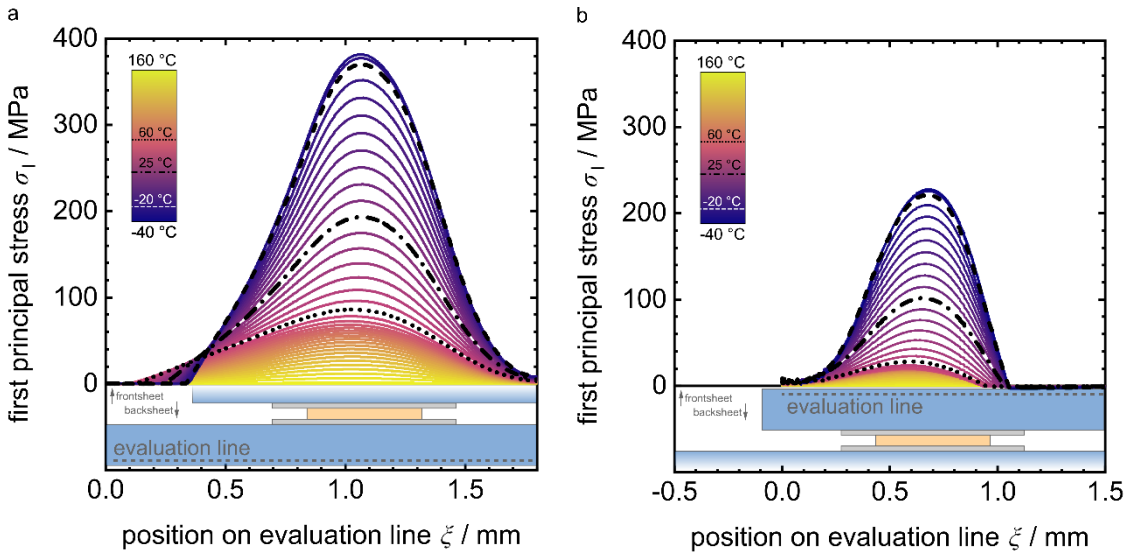

Figure 7: Evolution of σ_{I} along an evaluation line on **a** the rear side and **b** the front side of the solar cell with temperatures during cooling from $160\ °\mathrm{C}$ to $-40\ °\mathrm{C}$ (color code). Each line represents a temperature change of $5\ \mathrm{K}$. Room temperature is highlighted by the dot-dashed black line. $T_{\mathrm{g,ECA}} = 60\ °\mathrm{C}$ and $T_{\mathrm{g,EVA}} = -20\ °\mathrm{C}$ are highligted by a dotted and dashed line respectively.

Undoubtly, there is a significant gap between the computed stress amplitudes and the characteristic fracture stresses σ_{c} found for the solar cells. The question arises, why the observed cracks are not present at every ECA pad in every joint. For once there are significant differences between abstracted model geometry and manually manufactured modules in a laboratory. Different ECA pastes have different viscosities which ultimately lead to different ECA cross sections in size and shape (height and width). We also found in metallographic specimens, that the encapsulant infiltrates the solar call overlap to a varying extent (see e.g. void in Figure 3). The busbar geometry and positioning are far from being as ideal as accounted for in the FEM model and some rear side metallization features affecting the encapsulant filled gap between both solar cells are not considered at all.

Another important aspect are the material models. Linear viscoelasticity typically is considered to be valid up to $1\ \%$ strain. However, the computed strain amplitudes reach as high as $15\ \%$. Therefore, the missing non-linearity in the material model will overestimate the stresses. Also, inaccuracies in the time temperature superposition are a source of variance between model and reality (see. section 5.1). In summary, there are many variables affecting the experimental results, which cannot be account for in simulations adequately. Especially the height of the encapsulant filled gap between upper and lower

solar cell and also its CTE and storage modulus have a high impact on $\sigma_{\mathrm{I,max}}$. However, the qualitative match we found between model and simulation is remarkable and well suited to explain the driving mechanisms.

Bending moment

The high tensile stresses on the surface of the solar cells are caused by a bending moment in the joint. Figure 8 shows the characteristic distribution of y-normal stresses along a z-cross section in the center of the shingle joint. Both upper and lower solar cell feature a neutral axis close to their center with normal stresses increasing linearly towards the outer surfaces of the joint and linear increasing compressive stresses towards the ECA. The asymmetry between upper and lower cell again becomes visible in the peak values of σ_{y} which in this region equals σ_{I}. In the next paragraph, we will discuss the two mechanisms in the laminate causing the bending stresses and ultimately the crack formation.

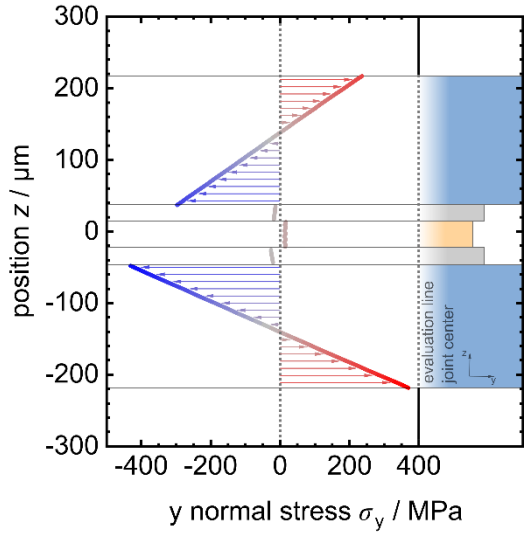

Figure 8: Distribution of normal stress σ_{y} along the evaluation line intersecting the joint center in z-direction.

Mechanisms behind the bending of solar cells at shingle joints

Two general mechanisms determine the formation of stresses in the module during cooling of the laminate.

First, the contraction of the laminate in y-direction. This mechanism is described in detail in the research of Eitner [2]. He found, that solar cells undergo a relative shift during cooling caused by the mismat of the CTEs of the materials in the laminate. Since front sheet and back sheet with $\alpha_{\mathrm{FS}} = 9 \cdot 10^{-6}\mathrm{K}^{-1}$ and $\alpha_{\mathrm{BS}} = 50 \cdot 10^{-6}\mathrm{K}^{-1}$ respectively contract stronger than the solar cells themselves ($\alpha_{\mathrm{Si}} \cong 3 \cdot 10^{-6}\mathrm{K}^{-1}$), the latter are shifted towards each other. Eitner proofed, that the gap displacement decreases along with the laminate temperature. We refer to this as the y-mechnism.

From such a behavior, an increasing overlap of the shingle solar cells during cooling follows. However, the ECA, filling the joint, hinders this movement which results in a bending of the solar cells around the joint. The hypothesis is, that this bending induces stresses that contribute to the crack formation.

The y-mechanism is sketched in Figure 9a. Note that for simplicity mechanical springs indicate the driving force for thermal strain.

The second mechanism follows from the thermal contraction of the materials in z-direction and subsequently is referred to as the z-mechanism. Figure 9b shows the essential processes. We consider two sections: First the region inside the overlap and second the region close, but outside the overlapping solar cells. Inside the overlap $\Delta\alpha_z$ between encapsulant and ECA causes a stronger contraction of the encapsulant. In the following, the free ends of the solar cells are pulled towards each other causing the solar cells in the overlap region to bend.

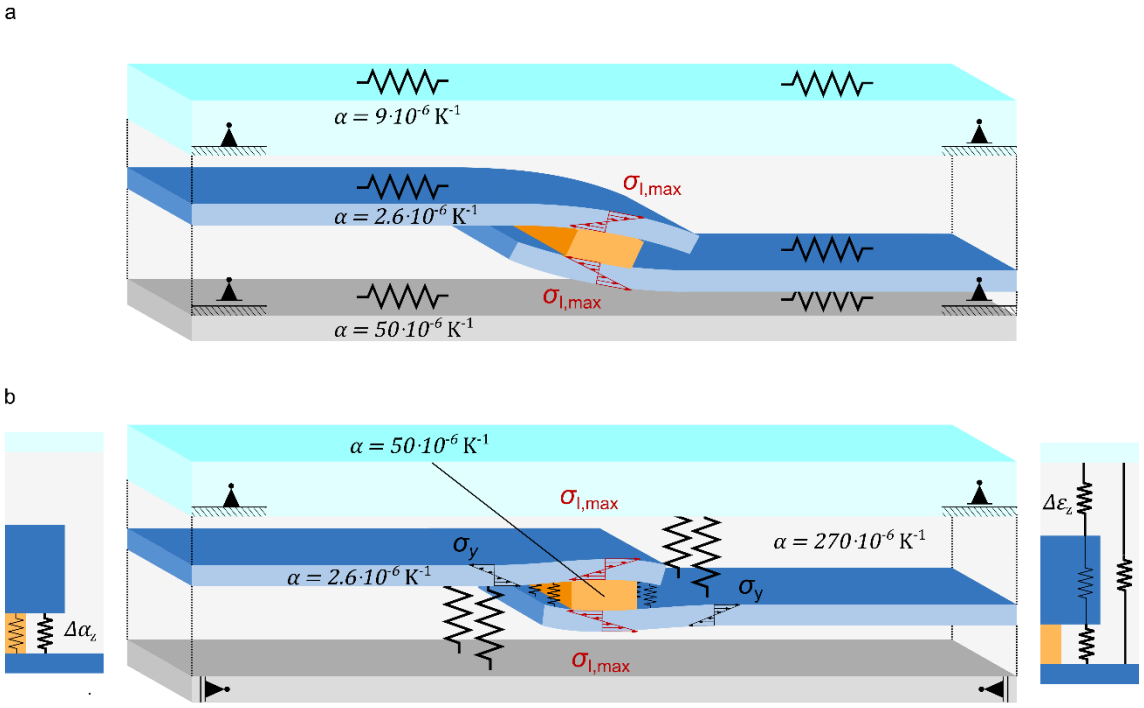

Figure 9: Simplified sketch of active forces around the shingle joint during cooling **a** impacts of the y-component of thermal contraction and therefore referred to as the y-mechanism **b** impacts of the z-component of thermal contraction and subsequently referred to as z-mechanism. Details showing the contraction inside the overlap and outside but close to the overlap.

At the edge of the overlap we identify two paths starting from the lower solar cell towards the front sheet. Along the first path approximately $40\ \%$ of the material is silicon while the second path purely consists of encapsulant. During cooling the path consisting of pure encapsulant will undergo higher contractions, which leads to a bending of the solar cell close to the overlap. Since the glass in good approximation is a fixed bearing in z-direction, the solar cell is pulled towards it. A likewise effect was discussed by Dietrich et al. [38] for ribbon based interconnection techniques.

In a similar manner, the upper solar cell is pulled towards the back sheet. However, since the back sheet is a thin and flexible polymer foil the bending of the solar cell is much less pronounced. In reverse conclusion we expect a symmetric bending of the solar cells in case of a glass-glass architecture (see appendix). Although we so far found no experimental evidence for solar cell cracking outside the

overlap, this mechanism provides the required precondition for cracks to also initiate close to the overlap.

Separation of the y- and z-mechanism

Since the stresses are based on thermal contraction occurring in different spatial directions, we separate the mechanisms in our numerical simulations by the implementation of anisotropic thermal expansion. For isotropic materials the thermal expansion follows $\boldsymbol{\alpha}_{\mathrm{iso}} = \boldsymbol{\alpha}_{\mathrm{x}} = \boldsymbol{\alpha}_{\mathrm{y}} = \boldsymbol{\alpha}_{\mathrm{z}}$ or $\boldsymbol{\alpha}_{\mathrm{iso}} = \alpha \boldsymbol{I}$ with the identity matrix $\boldsymbol{I}$. In the simulations anisotropic thermal expansion can be considered by the tensors given in Eq. (5) and Eq. (6). In the following we are comparing isotropic to anisotropic solutions of the FE model.

$$\boldsymbol{\alpha}_{\mathrm{y}} = \alpha \begin{pmatrix} 0 & 0 & 0 \\ 0 & 1 & 0 \\ 0 & 0 & 0 \end{pmatrix} \tag{5}$$

$$\boldsymbol{\alpha}_{\mathrm{z}} = \alpha \begin{pmatrix} 0 & 0 & 0 \\ 0 & 0 & 0 \\ 0 & 0 & 1 \end{pmatrix} \tag{6}$$

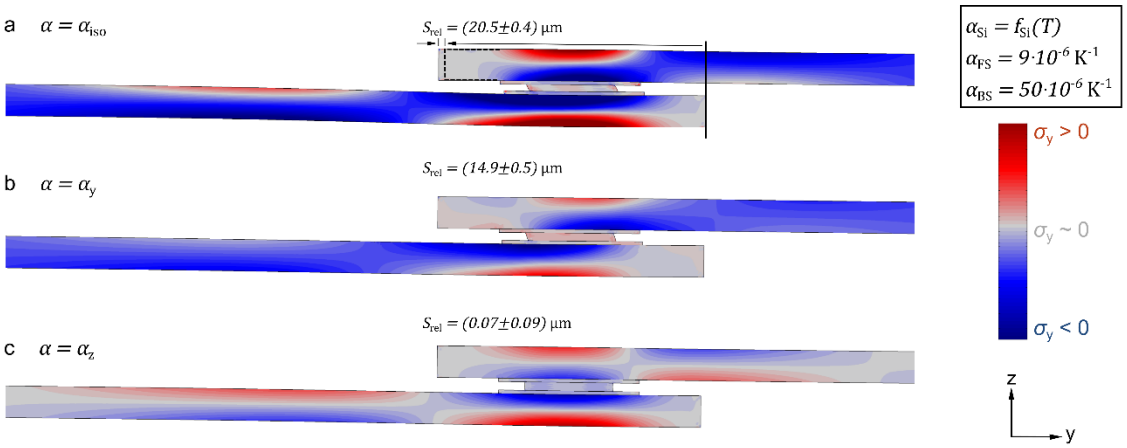

Figure 10: Distribution of normal stress σ_{y} in the solar cells close to the shingle joint for **a** isotropic and anisotropic thermal expansion **b** in y- and **c** in z-direction. In **a** the relative shift of the solar cells is defined as the change in the overlap width. The given errors correspond to the mean value found at all four joints the model.

Figure 10 shows the normal stress distributions in y-direction in the joint region for a thermal expansion tensor in case of a) isotropic thermal expansion, b) thermal expansion in y-direction and c) thermal expansion in z-direction. We define the relative shift of the solar cells as the difference of the overlapping length, as it is sketched in Figure 10a. Values $S_{\mathrm{rel}} > 0$ correspond to an increase and $S_{\mathrm{rel}} < 0$ to a decrease of the overlap. The given errors refer to the standard deviation of S_{rel} found at the joints in the FEM model.

As proposed in the mechanism (Figure 9a), we find that in case of a contraction in y-direction the solar cells shift towards each other and $S_{\mathrm{rel}} = (14.9 \pm 0.5)$ µm. The distribution of σ_{y} agrees with the y-mechanism and bending stresses occur dominantly at the shingle joint. Their maximal values are located slightly outside the center but still below and above the ECA in the joint.

For a pure z-contraction the solar cells are basically not shifting and becomes $S_{\mathrm{rel}} = (0.07 \pm 0.09)\ \mu\mathrm{m}$). Note the missing shear deformation of the ECA in the joint. We find two regions of distinct bending stresses. First within the overlap, we find an asymmetric bending of the solar cells with a more distinct bending of the lower solar cell. Second, just outside the overlap, we find bending stresses according to Figure 9b, again with an asymmetry and more distinct stress fields in the lower solar cell.

To further differentiate between their impact, we eliminate the y-mechanisms in our simulations. Eitner found, that the relative shift of ribbon-interconnected solar cells becomes close to zero, when the CTE of glass, backsheet and solar cells matches [2]. This is implemented in our simulations by solving the FE model for $\boldsymbol{\alpha}_{\mathrm{FS}} = \boldsymbol{\alpha}_{\mathrm{BS}} = \boldsymbol{\alpha}_{\mathrm{Si}} = f_{\mathrm{Si}}(T)$.

Two results can be expected: First, in case of $\boldsymbol{\alpha} = \boldsymbol{\alpha}_{\mathrm{z}}$ there should be no change in the result, since the thermal contraction of glass and back sheet in y-direction is not linked to the z-mechanism. Second, in case of $\boldsymbol{\alpha} = \boldsymbol{\alpha}_{\mathrm{y}}$ the solar cells are not shifting anymore ($S_{\mathrm{rel}} \cong 0$). Since the solar cell shift as driving force for the bending is eliminated, the bending stress distribution in σ_{y} vanishes.

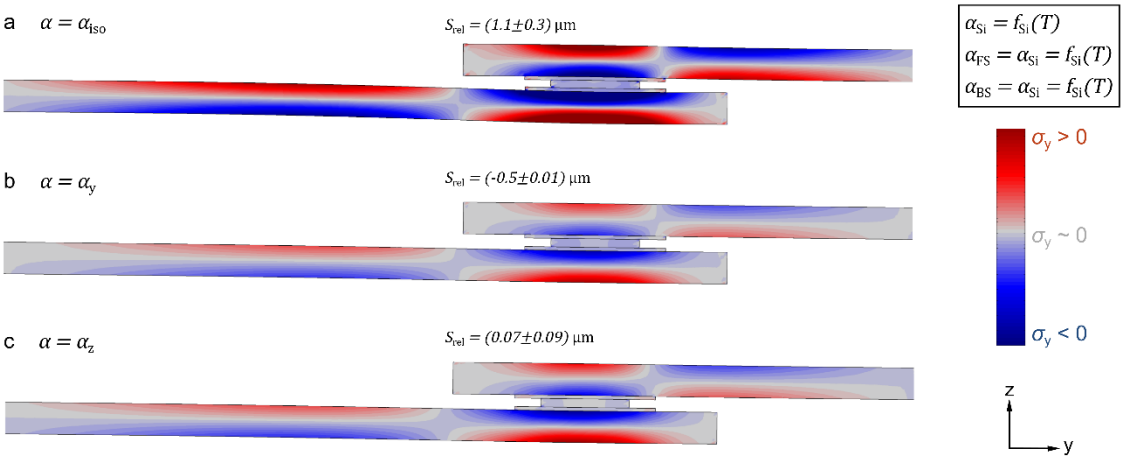

Figure 11: Distribution of normal stress σ_{y} in the solar cells close to the shingle joint for **a** isotropic and anisotropic thermal expansion **b** in y- and **c** in z-direction. In this computations the CTEs of glass and back sheet match the temperature dependent CTE of silicon to suppress S_{rel} for $\boldsymbol{\alpha} = \boldsymbol{\alpha}_{\mathrm{y}}$of the solar cells according to findings by Eitner [2].

Figure 11 shows the distribution of normal stress σ_{y} for matching CTEs again for a) the isotropic case b) thermal contraction only in y-direction and c) only in z-direction. The color scale is identical to the one used in Figure 10.

In case of $\boldsymbol{\alpha} = \boldsymbol{\alpha}_{\mathrm{z}}$ we find the solution to be like the one shown in Figure 10c and find our assumption confirmed: The CTE of glass and back sheet are not relevant for the z-mechanism

For $\boldsymbol{\alpha} = \boldsymbol{\alpha}_{\mathrm{y}}$ the relative shift S_{rel} becomes $\cong 0$. However, we still find bending stress distributions in and around the shingle joint. Furthermore, they now are similar to the ones for $\boldsymbol{\alpha} = \boldsymbol{\alpha}_{\mathrm{z}}$. This is caused by transversal contraction of the encapsulant. From Hooks law for isotropic materials Eq. (7) is derived for the z-strain. ν is the Poisson ratio for transversal contraction.

$$\varepsilon_{\mathrm{z,el}} = -\frac{\nu}{E}\sigma_{\mathrm{x}} - \frac{\nu}{E}\sigma_{\mathrm{y}} + \frac{1}{E}\sigma_z \tag{7}$$

When thermal expansion is present the strain tensor ε is a superposition of the elastic strain tensor $\varepsilon_{\mathrm{el}}$ and the thermal strain tensor $\varepsilon_{\mathrm{th}}$: $\varepsilon = \varepsilon_{\mathrm{el}} + \varepsilon_{\mathrm{th}}$. Inside the overlap the y strain of the encapsulant is constrained so that in an approximation $\varepsilon_{\mathrm{y}} = 0$. It follows, that $\varepsilon_{\mathrm{y,el}} \overset{!}{=} -\varepsilon_{\mathrm{y,th}}$ which again is responsible for a contraction component in z-direction according to Eq. (7). Hence, even without a thermal contraction in z-direction, a strain in z-direction is caused from transversal contraction. In the consequence the result is a similar bending of the solar cells as it is the case for a pure thermal contraction in z-direction only.

In summary, the comparison of the results for matched CTEs with the ones for material specific CTEs, shows clearly, that the root cause behind the observed cracks on the solar cell rear side is a z-contraction of the encapsulation material. We showed, that eliminating the lateral displacement of the shingle solar cells S_{rel} there are still large amplitudes of tensile stresses present. Their distribution is similar for both $\boldsymbol{\alpha}_{\mathrm{y}}$ and $\boldsymbol{\alpha}_{\mathrm{z}}$.

Contribution of the y-mechanism

Beyond the identification of the root cause for cracks, the simulations indicate another remarkable result regarding the y-mechanism. Figure 12 shows the comparison of σ_{I} on the rear side of the solar cell including the y-mechanism and without it being present.

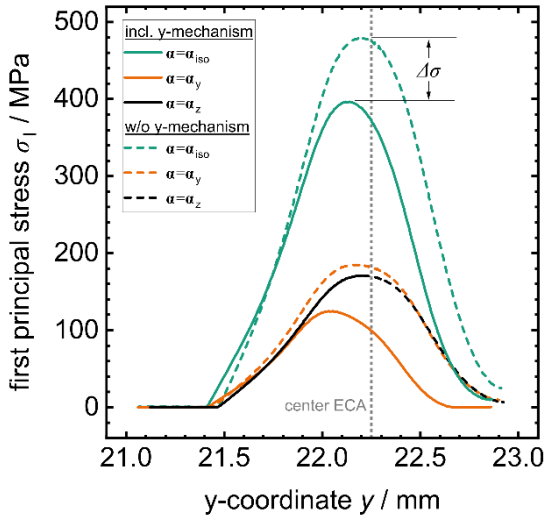

Figure 12: Stress distribution of σ_{I} for material specific CTEs resulting in a relative shift $S_{\mathrm{rel}} \neq 0$ *i.e.* including the y-mechanism and for matched CTEs eliminating S_{rel} (w/o y-mechanism). σ_{I} is evaluated close to the rear surface of lower solar cell (as sketched in Figure 7a) for the isotropic and both anisotropic cases of thermal expansion. Note that the data for $\boldsymbol{\alpha} = \boldsymbol{\alpha}_{\mathrm{z}}$ lie on top of each other and therefore in the figure only half of each data set is shown.

This evaluation shows again that the z-mechanism ($\boldsymbol{\alpha} = \boldsymbol{\alpha}_{\mathrm{z}}$, solid and dashed black line) is not affected by changes in the CTE of glass and back sheet. However, when comparing the course of σ_{I} in case of

$\boldsymbol{\alpha} = \boldsymbol{\alpha}_{\mathrm{y}}$, Figure 12 shows that the stress is reduced by $\Delta\sigma$ when the y-mechanism is present. We conclude that the y-mechanism not only is not responsible for the solar cell cracks but contrariwise it reduces the stresses caused by the z-mechanism. A reason could be stress fields at different positions which are mitigated by superposition of each individual contribution. The shift of the maximum value in y-direction is an indicator for this hypothesis.

Since the crack formation is mostly driven by the difference in contraction inside the joint, we propose the following strategies to reduce tensile stresses originating from bending:

- Reduce joint height. This will reduce the total difference in contraction and hence the absolute bending of the solar cells. This can be achieved with adjustments in the fabrication process.
- Increase the filling degree of the overlap with ECA. This can either be achieved by lowering the total overlap area or increasing the width of the ECA inside the overlap. This reduces the length of the free solar cell ends, which are pulled inwards by the encapsulant and can also be achieved by adjustments in the manufacturing process.
- Match the CTEs of encapsulant and ECA. This also reduces the mismatch in the total thermal contraction and thus leads to less bending of the solar cells. Since the CTE is an intrinsic and temperature dependent property of both materials, the implementation of this strategy is rather challenging.
- Reduce the mechanical stiffness of the ECA. In simulations using a scaling factor of 0.2 on the generalized Maxwell model results in a reduction of $\sigma_{\mathrm{I,max}}$ to $\sim 50\ \%$ of the initial value.

6 Conclusion

In this study we describe a so far non reported mechanism responsible for solar cell crack formation at shingle interconnections in PV modules. We investigated the crack formation experimentally in small scale modules with shingle strings interconnected by six different ECAs. We found that it occurs for five ECAs and conclude, that the mechanism is linked to the shingle joint itself. There are differences in the number of cracks counted for the different ECAs, but up to this point we cannot prove mechanical properties of the ECAs (like modulus or CTE) or variations in the joint geometry (like ECA height and width) to be responsible for this. However, it is likely, that the material properties play a crucial role in the defect occurrence.

We discuss two mechanisms of contraction in the laminate to be the root cause for bending and ultimately cracking of the solar cells in the joint region.

1. Thermal contraction in y-direction causes a relative shift of the solar cells, previously described for ribbon interconnected solar cells by Eitner [2]. In the shingle joint this shift is hindered by the ECA and subsequently is resulting in a bending of the solar cells.
2. Differences in thermal strain in z-direction inside and besides the overlap lead to bending of the solar cells.

Finite Element Analysis not only identifies the z-contraction to be the driving mechanism for cracking but also that the y-contraction mitigates the first principal stresses. The findings are in very good qualitative agreement with the results of the microscopic analysis of cross sections from the

experimentally investigated samples. Cracks originating from the rear surface of the solar cells in the center below the ECA joint are found in all metallographic specimens which showed the cracking also in luminescence imaging. The mechanism responsible for the cracking also shows that the coefficient of thermal expansion of the ECAs plays a crucial role. Matching the thermal contraction of the ECA with the thermal contraction of the encapsulant will reduce the stresses responsible for cracking.

We found that the cracks are not linked to significant losses in power. For one material system we find up to $50\,\%$ of the ECA pads with cracks, while the losses in power after TC1000 are only $(-2.3 \pm 1.5)\,\%$ and are related to a degradation of the fill factor and not the cell current. Nevertheless, cracked solar cells are much more likely to further degrade in combination with mechanical loads. Mechanical loads however cannot be considered adequately on the laboratory sized samples used in this study due to the size effect. Therefore, relevant and more crucial losses in power might occur on full-sized solar modules in the field, when mechanical loads apply.

Due to the high asymmetry in the laminate stack of glass-foil modules the defect occurs mostly on the rear side of the solar cells. Monofacial solar cells and opaque back sheets make a detection of the cracks challenging, since optical paths are needed for EL- or PL-imaging. We conclude that such cracks already may be present unnoticed in commercial shingle module products.

7 Acknowledgments

The author thanks all co-authors for their valuable contributions to this work. A special thanks goes to Andreas Beinert and Pascal Romer, which supported much of this work with criticism and fruitful discussions.

We thank the Federal Ministy of Economic Affairs and Energy (BMWi) for funding of this research under the contract number 03EE1026A, acronym Shirkan. We also thank the German Environmental Foundation (DBU) for supporting us within their graduate scholarship program.

8 Appendix

8.1 Material Models

8.1.1 Anisotropic Silicon

Table Appendix: Anisotropic material data for crystalline silicon and lattice orientations <100>, <010> and <001> corresponding to the cartesian coordinates x,y and z respectively

$C11$ [22]	165.6		
$C12$ [22]	63.9		
$C44$ [22]	79.5		
$E_x = E_y = E_z$ [20]	130		
$\nu_{xy} = \nu_{xz} = \nu_{yz}$ [20]		0.28	
$G_{xy} = G_{xz} = G_{yz}$ [20]	79.6		
			2.33 [22]
$T = 230\ K$ [23]		1.85	

$T = 270\ K$ [23]	2.33
$T = 310\ K$ [23]	2.69
$T = 340\ K$ [24]	2.87
$T = 380\ K$ [24]	3.11
$T = 400\ K$ [24]	3.21
$T = 500\ K$ [24]	3.39

8.1.2 Viscoelastic models

Table Appendix: Parameters of the Generalized Maxwell Model and the William-Landels-Ferry Shift function encapsulant and ECA.

Relaxation modulus / MPa			Relaxation constant / s			WLF parameters		
	EVA	ECA		EVA	ECA		EVA	ECA
G_0	0.21	5.07		-	-	T_{ref} / °C	−20.1	58.1
G_1	0.04	1.01	τ_1	9.04E-20	2.76E+06	C_1 / 1	54.4	92.5
G_2	0.06	2.51	τ_2	2.15E-15	1.84E+05	C_2 / °C	182	569.8
G_3	0.21	5.99	τ_3	1.00E-11	1.86E+04			
G_4	0.37	14.48	τ_4	8.16E-09	2.34E+03			
G_5	0.49	28.72	τ_5	1.61E-06	3.18E+02			
G_6	0.76	46.02	τ_6	8.61E-05	4.07E+01			
G_7	1.02	66.85	τ_7	2.73E-03	4.23E+00			
G_8	1.15	84.26	τ_8	6.15E-02	3.72E-01			
G_9	1.26	94.18	τ_9	1.25E+00	2.58E-02			
G_{10}	1.53	99.13	τ_{10}	2.31E+01	1.24E-03			
G_{11}	1.86	101.69	τ_{11}	3.92E+02	3.68E-05			
G_{12}	2.70	102.88	τ_{12}	8.85E+03	8.67E-07			
G_{13}	4.23	104.27	τ_{13}	2.27E+05	1.70E-08			
G_{14}	6.36	101.95	τ_{14}	7.20E+06	3.80E-10			
G_{15}	10.98	103.85	τ_{15}	3.03E+08	6.76E-12			
G_{16}	17.02	98.52	τ_{16}	1.15E+10	7.75E-14			
G_{17}	21.12	135.23	τ_{17}	4.01E+11	5.14E-16			
G_{18}	21.55	129.30	τ_{18}	1.10E+13	6.34E-18			
G_{19}	22.91	155.06	τ_{19}	1.90E+14	6.18E-20			
G_{20}	23.78	184.82	τ_{20}	3.00E+15	8.08E-22			
G_{21}	28.53		τ_{21}	5.47E+16				
G_{22}	34.30		τ_{22}	7.07E+17				
G_{23}	37.92		τ_{23}	9.80E+18				
G_{24}	41.30		τ_{24}	3.60E+20				
G_{25}	43.02		τ_{25}	3.07E+22				

8.2 BOM variations

After tracing back the bending of the solar cells to thermal contraction of the encapsulant materials in z-direction to be the driving mechanism behind the crack formation at shingle solar cell interconnections, we investigate variations in the bill of materials (BOM) on the mechanical stresses.

Since we observed that there is a significant stress concentration on the rear surface of the joint caused by the asymmetric layer stack in the glass-foil module, we first investigate the impact of a symmetric glass-glass architecture.

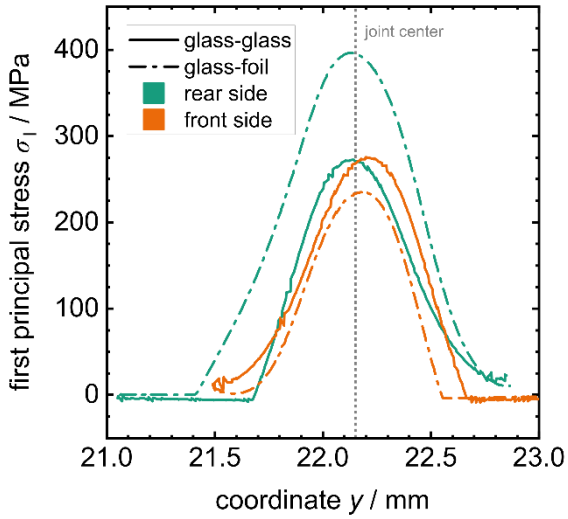

Figure 13 Distribution of σ_I in the overlap region comparing glass-glass and glass-foil modules. σ_I is evaluated close to the front and rear surface of the upper respectively lower solar cell, as sketched in Figure 7a.

Figure 13 shows the distribution of σ_I on the front and rear side of the solar cell. As expected, we find the symmetric layer sequence in glass-glass modules to cause symmetric stress distributions (continuous lines). However, the stresses in the solar cells are still quite high with (274.9 ± 3.6) MPa and (272.4 ± 2.9) MPa on front and rear side respectively. The error refers to the standard deviation of $\sigma_{I,max}$ found for all four joints. We conclude, that changing the module architecture to glass-glass architecture will reduce the stress on the solar cell rear side compared to the glass-foil architecture by approximately 120 MPa. However, glass-glass modules may also show the cracking of solar cells.

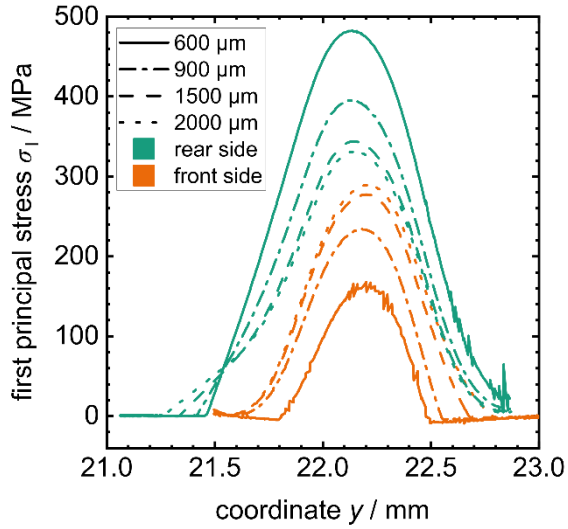

Figure 14: Stress distribution of σ_{I} in the overlap region for varied encapsulant thicknesses. σ_{I} is evaluated close to the front and rear surface of the upper respectively lower solar cell, as sketched in Figure 7a.

Another approach, often chosen in manufacturing, to reduce mechanical stresses, is the use of thicker encapsulant layers. Figure 14 shows the evolution of σ_{I} for an encapsulant with varied total thickness between $600\,\mu\mathrm{m}$ and $2000\,\mu\mathrm{m}$. The solar cells consequently are arranged in the center of the encapsulant. Like in the glass-glass architecture the stress becomes more symmetric with an increasing encapsulant thickness. $\sigma_{\mathrm{I,max}}^{\mathrm{RS}} = (485.0 \pm 4.1)\,\mathrm{MPa}$ at $600\,\mu\mathrm{m}$ is reduced to $\sigma_{\mathrm{I,max}}^{\mathrm{RS}} = (327.5 \pm 7.4)\,\mathrm{MPa}$ at $2000\,\mu\mathrm{m}$ encapsulant thickness. At the same time $\sigma_{\mathrm{I,max}}^{\mathrm{FS}}$ increases from $(172.4 \pm 3.7)\,\mathrm{MPa}$ to $(285.9 \pm 7.2)\,\mathrm{MPa}$. Ultimately, the stresses converge towards a value of around $300\,\mathrm{MPa}$. This is explained by the mechanical decoupling of the solar cells from front glass and back sheet, so that the bending mechanism in the joint is less affected by the outer layers.

9 References

[1] H. Wirth *et al.,* "Integrierte Photovoltaik: Aktive Flächen für die Energiewende," Fraunhofer Institute for Solar Energy Systems ISE, 2020.

[2] U. Eitner, "Thermomechanics of photovoltaic modules," Dissertation, Martin-Luther-Universität, Halle-Wittenberg, 2011.

[3] *Strength testing for photovoltaic wafers*, 91351, Deutsches Institut für Normung e.V. (DIN), Berlin, Apr. 2017.

[4] P. Baliozian, E. Lohmüller, T. Fellmeth, N. Wöhrle, A. Krieg, and R. Preu, "Bifacial p-type silicon shingle solar cells - the pSPEER concept," *Sol. RRL*, vol. 1700171, 1700171/1-1700171/5, 2018, doi: 10.1002/solr.201700171.

[5] N. Klasen, A. Mondon, A. Kraft, and U. Eitner, "Shingled Cell Interconnection: A New Generation of Bifacial PV-Modules," *7th Workshop on Metallization and Interconnection for Crystalline Silicon Solar Cells*, 2017, doi: 10.2139/ssrn.3152478.

[6] C. H. Schiller, L. C. Rendler, D. Eberlein, G. Mülhöfer, A. Kraft, and D. H. Neuhaus, "Accelerated TC Test in Comparison with Standard TC Test for PV Modules with Ribbon, Wire and Shingle Interconnection," in *Proceedings of the 36th European Photovoltaic Solar Energy Conference and Exhibition (EU PVSEC); Marseille, France*, 2019, pp. 995–999.

[7] M. Heinzelmann, *Versagensverhalten von einkristallinem Silizium an scharfen Kerben*. Düsseldorf: VDI-Verl., 1995.

[8] W. Weibull, *A Statistical Theory of the Strength of Materials*. Stockholm: Generalstabens Litografiska Anstalts Förlag, 1939.

[9] T. Hauck, C. Bohm, and W. H. Muller, "Weibull statistics for multiple flaw distributions and its application in silicon fracture prediction," in *Thermal, Mechanical and Multi-Physics Simulation*

and Experiments in Micro-Electronics and Micro-Systems, 2005. EuroSimE 2005. Proceedings of the 6th International Conference on, 2005, pp. 242–247.

[10] I. PAUL, B. MAJEED, K. RAZEEB, and J. BARTON, "Statistical fracture modelling of silicon with varying thickness," *Acta Materialia*, vol. 54, no. 15, pp. 3991–4000, 2006, doi: 10.1016/j.actamat.2006.04.032.

[11] C. V. Schmid, "Schadensmechanismen bei Silizium-Solarzellen und Maßnahmen zur Festigkeitserhöhung," Dissertation, Fakultät für Maschinenbau, Karlsruher Institut für Technologie, Karlsruhe, 2010.

[12] A. J. Beinert, P. Romer, M. Heinrich, M. Mittag, J. Aktaa, and H. Neuhaus, "The Effect of Cell and Module Dimensions on Thermomechanical Stress in PV Modules," *IEEE J. Photovoltaics*, vol. 10, no. 1, pp. 70–77, 2020, doi: 10.1109/JPHOTOV.2019.2949875.

[13] *Hochleistungskeramik - Monolithische Keramik - Mechanische Eigenschaften bei Raumtemperatur: Teil 5: Statistische Auswertung*, DIN EN 843-5, Deutsches Institut für Normung e.V. (DIN), Jan. 2005.

[14] F. Kaule, M. Pander, M. Turek, M. Grimm, E. Hofmueller, and S. Schoenfelder, "Mechanical damage of half-cell cutting technologies in solar cells and module laminates," in *SiliconPV 2018, The 8th International Conference on Crystalline Silicon Photovoltaics: Conference date, 19-21 March 2018 : location, Lausanne, Switzerland*, 2018, p. 20013.

[15] F. Kaule, W. Wang, and S. Schoenfelder, "Modeling and testing the mechanical strength of solar cells," *Sol Energ Mat Sol C*, 120, Part A, pp. 441–447, 2014, doi: 10.1016/j.solmat.2013.06.048.

[16] S. Eiternick *et al.,* "High Quality Half-cell Processing Using Thermal Laser Separation," *Enrgy Proced*, vol. 77, pp. 340–345, 2015, doi: 10.1016/j.egypro.2015.07.048.

[17] *Terrestrial photovoltaic (PV) modules – Design qualification and type approval – Part 1-1: Special requirements for testing of crystalline silicon photovoltaic (PV) modules*, IEC 61215-1-1, International Electrotechnical Commission (IEC), Geneva, Switzerland, 2016.

[18] S. Dietrich, "Numerische Untersuchungen zur mechanischen Zuverlässigkeit verkapselter Siliziumsolarzellen," Dissertation, Fakultät für Maschinenbau, Otto-von-Guericke-Universität Magdeburg, Halle (Saale), 2014.

[19] J. Zarzycki and R. W. Cahn, Eds., *Materials science and technology: A comprehensive treatment*. Weinheim: VCH, 1991.

[20] M. A. Hopcroft, W. D. Nix, and T. W. Kenny, "What is the Young's Modulus of Silicon?," *J. Microelectromech. Syst.*, vol. 19, no. 2, pp. 229–238, 2000.

[21] S. Wiese, F. Kraemer, E. Peter, and J. Seib, "Mechanical problems of novel back contact solar modules," in *Proceedings of the 13th IEEE International Conference on Thermal, Mechanical and Multi-Physics Simulation and Experiments in Microelectronics and Microsystems*, Cascais,

Portugal, 2012, 1-6. [Online]. Available: http://ieeexplore.ieee.org/stamp/stamp.jsp?arnumber=6191770

[22] J. J. Hall, “Electronic Effects in the Elastic Constants of n -Type Silicon,” *Phys. Rev.*, vol. 161, no. 3, pp. 756–761, 1967, doi: 10.1103/PhysRev.161.756.

[23] K. G. Lyon, G. L. Salinger, C. A. Swenson, and G. K. White, “Linear thermal expansion measurements on silicon from 6 to 340 K ,” *J Appl Phys*, vol. 48, no. 3, pp. 865–868, 1977, doi: 10.1063/1.323747.

[24] Y. Okada and Y. Tokumaru, “Precise determination of lattice parameter and thermal expansion coefficient of silicon between 300 and 1500 K,” *J Appl Phys*, vol. 56, no. 2, pp. 314–320, 1984, doi: 10.1063/1.333965.

[25] “CRC Handbook of Chemistry and Physics: A Ready-Reference of Chemical and Physical Data, 85th ed Edited by David R. Lide (National Institute of Standards and Technology). CRC Press LLC: Boca Raton, FL. 2004. 2712 pp. $139.99. ISBN 0-8493-0485-7,” *Journal of the American Chemical Society*, vol. 127, no. 12, p. 4542, 2005, doi: 10.1021/ja041017a.

[26] N. Klasen, P. Romer, A. J. Beinert, and A. Kraft, “FEM Simulation of Deformations in Strings of Shingled Solar Cells Subjected to Mechanical Reliability Testing,” in *AIP Conference Proceedings 2156*, Konstanz, 2019, 020016-1–020016-11.

[27] M. Pander, S. Dietrich, S.-H. Schulze, U. Eitner, and M. Ebert, “Thermo-mechanical assessment of solar cell displacement with respect to the viscoelastic behaviour of the encapsulant,” in *Proceedings of the 12th IEEE International Conference on Thermal, Mechanical and Multi-Physics Simulation and Experiments in Microelectronics and Microsystems*, Linz. Austria, 2011, pp. 1–6.

[28] M. Springer and N. Bosco, “Linear viscoelastic characterization of electrically conductive adhesives used as interconnect in photovoltaic modules,” *Prog. Photovolt: Res. Appl.*, vol. 42, p. 38, 2020, doi: 10.1002/pip.3257.

[29] N. W. Tschoegl, Ed., *The Phenomenological Theory of Linear Viscoelastic Behavior*. Berlin, Heidelberg: Springer Berlin Heidelberg, 1989.

[30] J. D. Ferry, *Viscoelastic Properties of Polymers,* 3rd ed.: Wiley, 1980.

[31] I. M. Ward and J. Sweeney, *Mechanical properties of solid polymers*. Chichester, West Sussex, United Kingdom: Wiley, 2013.

[32] R. S. Lakes, *Viscoelastic solids*. Boca Raton: CRC Press, 1999.

[33] M. L. Williams, R. F. Landel, and J. D. Ferry, “The Temperature Dependence of Relaxation Mechanisms in Amorphous Polymers and Other Glass-forming Liquids,” *Journal of the American Chemical Society*, vol. 77, no. 14, pp. 3701–3707, 1955, doi: 10.1021/ja01619a008.

[34] M. Pander, S.-H. Schulze, and M. Ebert, “Mechanical Modeling of eletrically conductive Adhesives for photovoltaic Applications,” in *Proceedings of the 29th European Photovoltaic Solar Energy Conference and Exhibition*, Amsterdam, Netherlands, 2014, pp. 3399–3405.

[35] M. Stommel, M. Stojek, and W. Korte, *FEM zur Berechnung von Kunststoff- und Elastomerbauteilen,* 2nd ed. München: Hanser, 2018.

[36] O. C. Zienkiewicz, J. Z. Zhu, and R. L. Taylor, *The finite element method: Its basis and fundamentals*. Oxford, UK: Butterworth-Heinemann, 2013. [Online]. Available: http://site.ebrary.com/lib/alltitles/docDetail.action?docID=10755372

[37] *Plastics. Thermomechanical analysis (TMA). Determination of coefficient of linear thermal expansion and glass transition temperature*, BS ISO 11359-2:1999, British Standards Institution, Nov. 1999.

[38] S. Dietrich, M. Pander, M. Sander, U. Zeller, and M. Ebert, “Stress analysis of encapsulated solar cells by means of superposition of thermal and mechanical stresses,” in *Proc. of SPIE*, 882505-1-882505-10.